Scientific Research Publishing

Advances in Materials Physics and Chemistry, 2026, 16(4), 145-160
https://www.scirp.org/journal/ampc
ISSN Online: 2162-5328
ISSN Print: 2162-531X

Synthesis and Characterization of Copper Dendritic Structures Obtained by Electrocrystallization at High Current Density

Yauheni Shmatok[1*], Ekaterina Muratova[1], Igor Vrublevsky[2], Vyacheslav Moshnikov[1]

[1]Department of Micro- and Nanoelectronics, Saint Petersburg Electrotechnical University "LETI", Saint Petersburg, Russia
[2]R&D Laboratory of Multifunctional Metal Oxide Composite Materials, BSUIR, Minsk, Belarus
Email: *yauheni.shmatok@gmail.com

How to cite this paper: Shmatok, Y., Muratova, E., Vrublevsky, I. and Moshnikov, V. (2026) Synthesis and Characterization of Copper Dendritic Structures Obtained by Electrocrystallization at High Current Density. *Advances in Materials Physics and Chemistry*, **16**, 145-160.
https://doi.org/10.4236/ampc.2026.164007

Received: March 12, 2026
Accepted: April 11, 2026
Published: April 14, 2026

Abstract

Dendritic copper structures were synthesized by electrocrystallization from a sulfate electrolyte (0.31 M $CuSO_4$ + 1.53 M H_2SO_4) at a high cathode current density of 20 A/dm^2 under conditions of concurrent hydrogen evolution. The obtained deposits are approximately 200 μm in thickness. The multilevel void architecture of the dendritic copper was characterized using scanning electron microscopy combined with image processing and statistical analysis. Interdendritic voids were approximated by area-equivalent fitted ellipses, enabling quantitative assessment of pore size distributions. Analysis by quantity revealed three distinct void populations with peak maxima at 2.41 μm, 5.06 μm, and 10.93 μm, accounting for 23%, 34%, and 42% of voids, respectively. Area-weighted analysis identified four void populations with peak maxima at 15.9 μm, 33.4 μm, 46.0 μm, and 72.2 μm, contributing 54%, 16%, 19%, and 4% of the total void area. The estimated pore density was 2529 pores/mm^2, the total void area fraction was found to be 0.3054, with an average void area of 108.46 μm^2 corresponding to an effective diameter of 11.75 μm. A distinct category of through-pores was identified, defined as voids with an effective diameter ≥ 20 μm through which the underlying substrate surface becomes visible in SEM images. These through-pores, formed by the coalescence of hydrogen bubbles generated during the hydrogen evolution reaction, occupy approximately 39% of the total void area and provide significantly enhanced filtration and diffusion characteristics compared to smaller pores. The hierarchical void structure, combining numerous small pores for high surface area with larger interconnected channels for efficient transport, makes these dendritic copper films promising candidates for application as current collectors in lithium-ion batteries.

Keywords

Copper Dendrites, Electrocrystallization, High Current Density, Image Analysis, Pore Size Distribution, Through-Pores

1. Introduction

The electrodeposition of copper dendritic structures has attracted considerable research interest due to their unique morphological features and promising applications in various electrochemical systems. When electrodeposition is conducted under high current density conditions, particularly in the presence of concurrent hydrogen evolution, the resulting copper dendrites exhibit complex multilevel architectures with well-developed interdendritic void networks [1]-[3]. Younus *et al.* [1] demonstrated that a two-step electrodeposition approach creating 3D porous trimetallic alloys begins with the electrodeposition of 3D copper dendrites, which was found to be crucial for the catalyst's mechanical stability. Their Cu@Cu-Ni-Co catalyst maintained remarkable stability in both acidic and neutral conditions at high current densities (48 - 165 $mA \cdot cm^{-2}$) for up to 50 h without any decline in activity, highlighting the importance of the developed electrodeposition approach [1]. Dixon *et al.* [2] demonstrated that nanoporous copper fabricated from CuZn alloy precursors exhibits significant surface area enhancements, corresponding to a surface-area-to-volume ratio of 2.3×10^6 cm^{-1} at the macro-scale and 4.9×10^5 cm^{-1} at the micro-scale, a 289-fold and 47-fold increase over their respective geometric surface areas. Their findings highlighted the need for scale-specific bath optimisation to enable reliable nanoporous copper formation [2]. Furthermore, Guo *et al.* [3] developed a simple and efficient electrodeposition-chemical dealloying process to fabricate a relatively high-porosity, high-performance porous copper current collector with a thickness of 12 μm, a porosity of 36.9%, and a mechanical strength of 362 MPa. Electrochemical tests showed that the Coulombic efficiency of the half-cell remained 98.05% after 240 cycles, and the de-alloyed porous copper current collector demonstrated more excellent Coulombic efficiency and cycle stability compared to commercial foil [3]. The interdendritic void network in such structures presents a sophisticated multilevel topology, where primary pores formed by hydrogen bubble templates are interconnected with secondary dendritic interspaces, creating a highly developed three-dimensional architecture that significantly enhances the electrochemically active surface area [3].

The unique topological features of dendritic copper structures make them exceptionally suitable for application as current collectors in lithium-ion batteries, where high surface area and porous architecture are critical for electrode performance. Liang *et al.* [4] prepared a lithiophilic Ag-3D-Cu collector by electroless silver plating on the surface of foam copper. The Ag-3D-Cu-30 s electrode obtained after a chemical silver-plating time of 30 s exhibited a lower overpotential

for nucleation and polarization compared to 3D-Cu electrodes while achieving a uniform lithium deposition morphology. The Li||Ag-3D-Cu-30 s cell showed stable cycling for nearly 140 cycles, with an average Coulombic efficiency of 98%, demonstrating excellent cycling performance [4]. Wang *et al.* [5] developed mulberry-like copper foil (M-CF) with a biomimetic structure on the surface of copper foil by adsorbing poly (acrylic acid) molecules on the surface of copper to hinder and disperse its growth during electrodeposition, optimizing its growth mode. The M-CF anode was capable of stable Li plating/stripping over 500 cycles with a high average Coulombic efficiency of 98.1%. The assembled symmetrical battery was stably cycled over 1600 h at a low voltage hysteresis of 11 mV [5]. Beyond these battery-specific studies, various electrodeposition approaches have been explored to create porous copper architectures. Younus *et al.* [1] employed a two-step electrodeposition method to create 3D porous Cu@Cu-Ni-Co alloys, where initial copper dendrite deposition proved crucial for mechanical stability, achieving an overpotential of 275 mV at 10 $mA \cdot cm^{-2}$ in phosphate-buffer solution.

Together with developing topologically new dendritic structures, some of the researchers are improving their experimental studies with various characterization techniques [2] [6]. Dixon *et al.* [2] utilized citrate-complexed sulphate baths for electrodeposition of CuZn alloy precursors followed by chemical dealloying, with physical characterisation using SEM, AFM, EDX, XRD, and TEM confirming the formation of nanoporous architectures with consistent crystallographic features across scales. Colliard-Granero *et al.* [6] developed deep-learning-enabled 3D analysis methods for porous materials in energy devices, demonstrating that traditional analytical techniques such as 2D scanning electron microscopy followed by Otsu thresholding and manual annotation lack the three-dimensional context necessary to accurately capture complex physical properties of porous electrode media.

The efficiency of battery current collectors is fundamentally determined by their specific surface area, which is intimately related to void size parameters, including pore size distribution and overall porosity. Accurate determination of these parameters requires specialized characterization techniques and equipment. Lv *et al.* [7] demonstrated that physisorption techniques provide detailed insights into pore structure, offering specific surface area (BET), pore volume, and pore size distribution data, though collection of a complete isotherm can require approximately 9 hours per sample, with micropore size distribution analysis taking about 1.5 hours. Dixon *et al.* [2] employed scanning electron microscopy combined with image analysis to characterize the porous structure of three-dimensional current collectors, systematically investigating the effects of substrate copper foil condition and electrodeposition parameters on the microstructure and properties of the alloy coating. Colliard-Granero *et al.* [6] developed UTILE-Pore, a deep-learning-enabled 3D analysis method, demonstrating that their approach captures the complex three-dimensional morphology of porous materials that traditional 2D

techniques miss, but such approach requires a sufficient quantity of 3D micro-CT data for training and calibration.

The aim of this work was to synthesize, study, and characterize the void structure of dendritic copper films, obtained by electrocrystallization at high current density, employing image processing and statistical distribution analysis as an alternative, time-effective, and cost-effective characterization approach. This methodology enables quantitative assessment of pore architecture, including pore size distribution, porosity, and morphological parameters directly from microscopic images, providing a rapid screening tool that can serve as a pre-test characterization technique. Such analysis allows researchers to identify which samples warrant further detailed electrochemical testing, potentially reducing the time and resources dedicated to exhaustive characterization of unsuitable specimens while enabling informed selection of optimal dendritic structures for battery current collector applications.

2. Experimental Part

The electrodeposition of copper in the form of dendritic structures was performed via electrolysis of Cu^{2+} ions onto a copper substrate measuring 100 × 20 × 1 mm (supplied by Shandong Hongyan Metal Material Co., Ltd.). The substrates were commercially pure flat plates of grade C11000, containing a minimum of 99.90% Cu, approximately 0.02% to 0.06% O_2, with the balance comprising trace elements. The electrodeposition process was conducted in an electrolyte composed of 0.31 M $CuSO_4$ and 1.53 M H_2SO_4, at a voltage of 3.6 V and a cathode current density of 20 A/dm^2 for a duration of 2.5 hours. A custom-designed three-electrode cell was used (**Figure 1**), featuring two anodes and one cathode positioned centrally between them. This configuration ensures a more uniform current distribution across the cathode surface compared to two-electrode cell. The electrolyte volume of the cell was filled with approximately 3.6 … 4 liters of freshly prepared electrolyte. To improve the uniformity of copper deposition, especially at high current densities, the cathode was mechanically moved during the deposition process, as shown in **Figure 1**. Such linear reciprocation motion, with an amplitude of 40 mm and frequency of 10 rpm, enhances mass transport and disrupts the diffusion boundary layer.

A programmable DC power supply, GW Instek SPD-3606 (Good Will Instrument, Taiwan region), was used in galvanostatic (constant current) mode.

To ensure deposition occurred only on the front surface, the reverse side of the plate was protected with insulating tape. Following deposition, the obtained samples, featuring a dendritic copper layer approximately 200 μm thick, were carefully rinsed with running distilled water (**Figure 2**).

A total of 1983 voids were segmented and analyzed from a single representative SEM field, providing the statistical basis for the distribution functions presented in this study. Ten independently prepared samples were examined across 67 SEM fields to confirm the representative nature of the analyzed image.

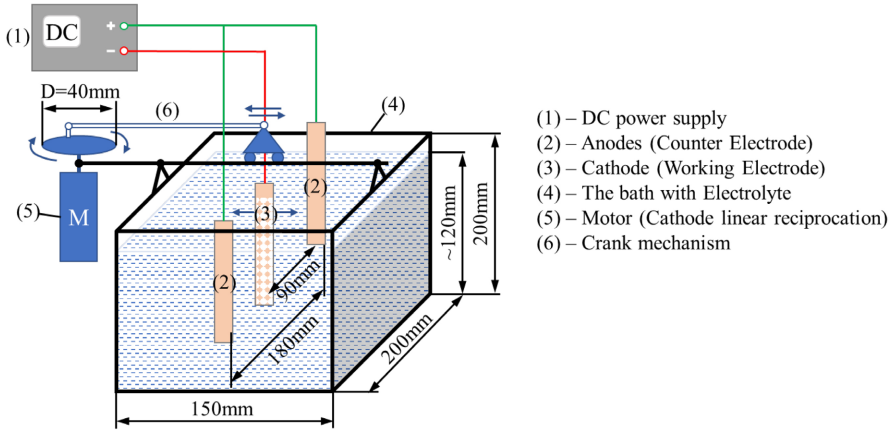

Figure 1. Schematic diagram of electrodeposition setup.

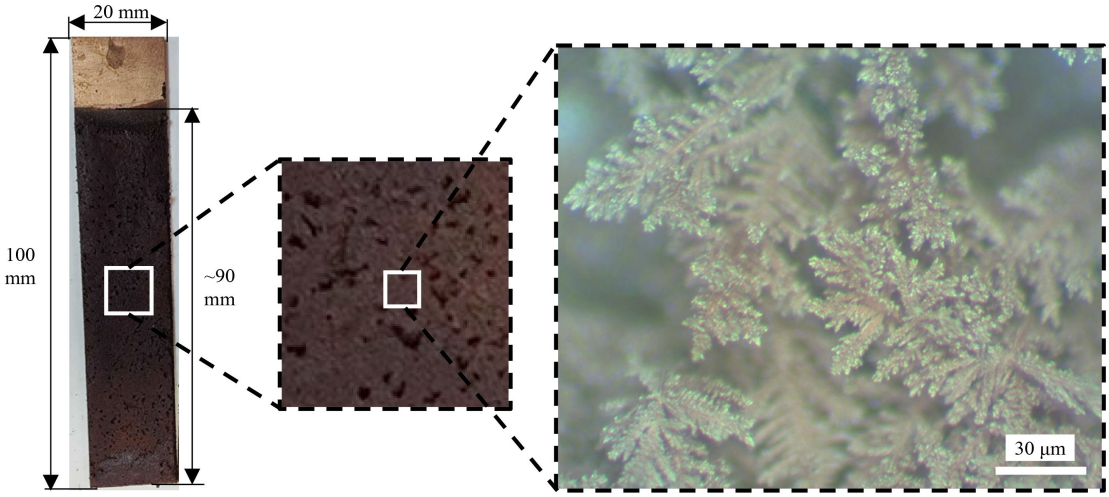

Figure 2. Sample appearance.

The surface morphology of the obtained Cu dendrites was examined using scanning electron microscopy (SEM) with a ZEISS EVO 10 instrument (Germany). A representative SEM image of the dendritic surface morphology is presented in **Figure 3(a)**. To facilitate quantitative analysis, the SEM image was processed using ImageJ software to generate a binary image (**Figure 3(b)**). The threshold value for binarization was set manually to ensure high-resolution representation of the interdendritic (void) space. Subsequently, the interdendritic spaces, appearing white in the binary image, were approximated by area-equivalent fitted ellipses (**Figure 3(c)**). The orientation of each ellipse was defined such that its major axis aligned with the shortest distance between the two most distant pixels of the corresponding void area. Each fitted ellipse was characterized by three primary metrics (**Figure 3(c)**): the length of the major axis *a*, the length of the minor axis *b*, and the inclination angle of the major axis relative to the horizontal (X-axis). Using these metrics, the area $A = \pi ab$, aspect ratio a/b, and eccentricity of each ellipse were calculated and compiled in Microsoft Excel. The effective diameter of each void was defined as the diameter of a circle with equivalent area: $d_{eff} = 2\sqrt{A/\pi}$. This

scalar value allowed direct comparison of void sizes irrespective of shape. A through-pore was operationally defined as a void with $d_{eff} \geq 20$ μm, based on the observation that voids of this size or larger consistently revealed the substrate surface beneath the dendritic layer in SEM images.

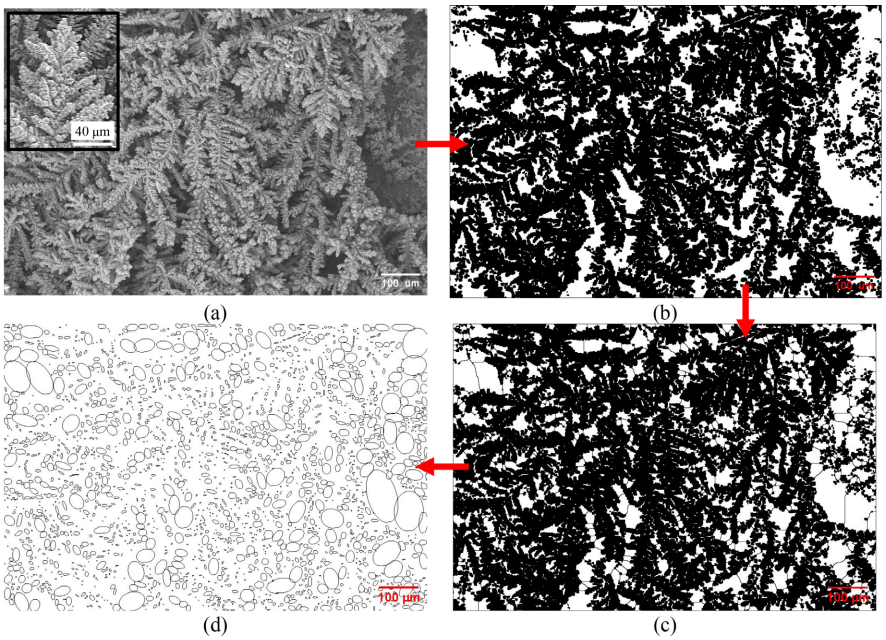

Figure 3. Reference image and processing results: (a) SEM image of the copper dendrites (Insert: single dendrite branch); (b) Binary mask; (c) Segmented binary mask using watershed; (d) Map of fitted ellipses into the void space of the segmented binary mask.

Further statistical analysis, including the computation of probability distribution functions and their normalization, was also performed in Excel. The resulting normalized cumulative distribution function (CDF) curves were subsequently processed using Origin software, employing the peak fit module to perform deconvolution of the CDF curves, thereby enabling detailed identification of predominant pore populations and their respective fractions.

3. Results and Discussion

3.1. Image Processing

It is known that the volume of voids in Cu-dendrites formed during the electrolytic deposition method is multileveled [8]-[10]. The formation of a multilevel void structure indicates that certain areas of the cathode experience difficulty with the supply of copper ions during electrodeposition, and the processes of discharge of copper and hydrogen ions occur at spatially separated locations. The centers of such areas were apparently sites of preferential discharge of hydrogen ions, which after reduction, formed gas bubbles, effectively blocking the supply of copper ions to those regions. The developed morphology of copper dendrites was analyzed by characterizing interdendritic voids through representing them as elliptical equiv-

alents, where each ellipse has an area equal to that of the replaced void region.

The SEM image of the dendritic structure with the three studied types of voids is shown in **Figure 3(a)**. Visual examination reveals a highly porous architecture characterized by interconnected dendritic branches and complex void networks of varying sizes and morphologies.

The characterization of the binary mask (**Figure 3(b)**) begins with a segmentation procedure, the result of which is presented in **Figure 3(c)**. Segmentation was performed using the watershed algorithm to properly separate overlapping or interconnected void regions, ensuring that each individual void could be analyzed independently. Following segmentation, an ellipse-fitting algorithm based on the method of moments [11] [12] was applied to each identified void region. This approach generates a map of ellipses that optimally represent the geometry of each void space while preserving the area equivalence principle (**Figure 3(d)**). Each fitted ellipse retains the spatial orientation and aspect ratio characteristics of the original void, enabling comprehensive morphological analysis.

From the resulting ellipse map, the estimated pore density was calculated to be 2529 pores per square millimeter, indicating a highly developed porous architecture with a dense distribution of interdendritic voids. The total void area fraction, obtained directly from the binary image (**Figure 3(b)**) as the ratio of white (void) pixels to total pixels, was found to be 0.3054. This value represents the overall porosity of the dendritic layer in the analyzed plane and provides a fundamental morphological parameter that complements the pore size distribution analysis.

Based on the ensemble statistics of all fitted ellipses, the average area of the inscribed ellipses was determined to be 108.46 μm^2. This value corresponds to an effective pore diameter of 11.75 μm, calculated as the diameter of a circle with equivalent area. This effective diameter provides a convenient single-parameter representation of the characteristic void size within the dendritic copper structure.

The multilevel nature of the void architecture, previously suggested in the literature [8]-[10], is visually confirmed by the variety of ellipse sizes visible in **Figure 3(d)**. The presence of both large primary voids (likely formed by hydrogen bubble templates during electrodeposition) and smaller secondary voids (originating from the spaces between individual dendritic branches) contributes to the hierarchical pore structure. This multiscale porosity is particularly advantageous for electrochemical applications, as it provides both high specific surface area from small pores and efficient electrolyte transport pathways through larger interconnected channels.

The quantitative approach presented here—combining SEM imaging, binary segmentation, watershed separation, and ellipse fitting—enables objective and reproducible characterization of complex dendritic morphologies. Unlike qualitative visual assessment, this method yields statistically robust metrics that can be correlated with synthesis parameters and ultimately with electrochemical performance.

3.2. Distribution Functions of Fitted Ellipses, Built by Quantity

Using the equations of mathematical statistics [13] [14], normalized graphs of the probability distribution function (PDF) were constructed—representing the differential distribution—along with the cumulative distribution function (CDF) of the ellipses, representing the integral distribution (Figure 4). The obtained curves were constructed based on the number of ellipses falling within a limited range of areas, recalculated as the Effective Diameter of voids. The Effective Diameter of voids is a scalar value derived from the area of each fitted ellipse, representing the diameter of a circle with equivalent area.

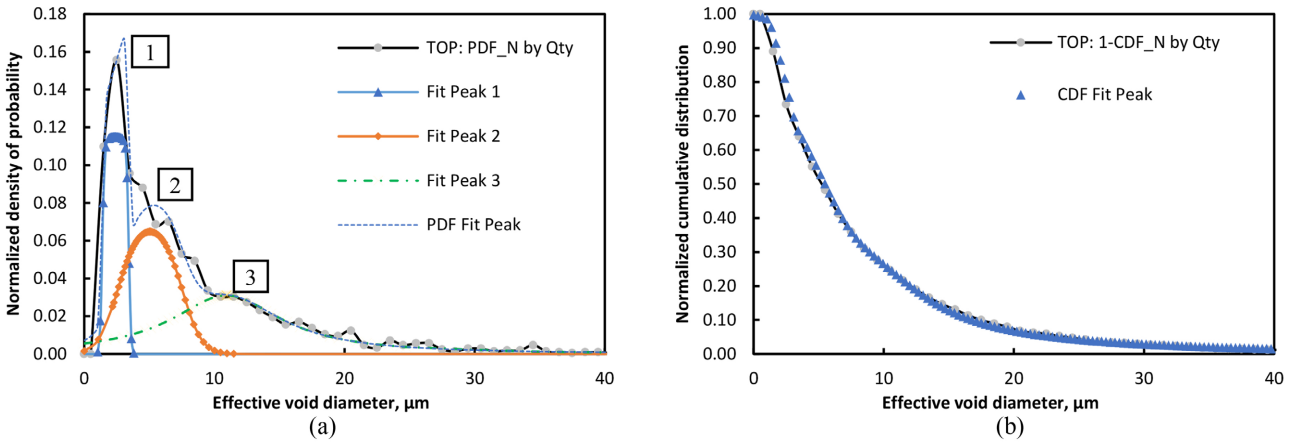

Figure 4. Distribution functions of fitted ellipses based on quantity: (a) Probability density function (PDF) with deconvoluted peaks; (b) Complementary cumulative distribution function (1-CDF).

The PDF function shown in Figure 4(a) exhibits feature characteristics of multimodal distributions, which upon deconvolution, reveal three underlying populations of voids. Peak fitting was performed in Origin software using the Gaussian_LorenCross peak type, which combines Gaussian and Lorentzian contributions for optimal representation of the experimental data. Selected from among the Gaussian-based models, it yielded the highest fit accuracy, as confirmed by the coefficient of determination ($R^2 = 0.99$). The number of peaks was chosen by minimizing the residual sum of squares while avoiding overfitting; three peaks provided an optimal balance between fit quality and model parsimony. The deconvolution parameters are summarized in Table 1.

Table 1. Deconvolution data summary of quantity-based PDF.

Peak Number	1	2	3
Effective void diameter by peak maximum, µm	2.41	5.06	10.93
Fraction	0.23	0.34	0.42
Full width at half maximum (FWHM), µm	2.03	5.1	10.3
R-sqr (COD)		0.99	

The deconvolution analysis reveals three distinct void populations within the dendritic copper structure. The first population, centered at an effective diameter of 2.41 μm, represents the smallest voids with a relatively narrow size distribution (FWHM = 2.03 μm). This population accounts for approximately 23% of the total void quantity and likely corresponds to the spaces formed between individual dendritic branches during the early stages of crystal growth.

The second population, centered at 5.06 μm with a FWHM of 5.10 μm, constitutes the largest fraction (34%) of voids by quantity. This intermediate population represents the primary interdendritic spaces formed during the main growth phase of the electrodeposition process.

The third population, centered at 10.93 μm with a substantially broader distribution (FWHM = 10.30 μm), accounts for the largest proportion (42%) of voids by quantity. Despite being the most numerous, this population exhibits the widest size variability. These large voids likely originate from regions where hydrogen bubble formation temporarily blocked copper ion supply during electrodeposition, creating larger cavities within the dendritic architecture. The excellent fit quality ($R^2 = 0.99$) confirms that the three-population model accurately represents the underlying void size distribution.

The complementary cumulative distribution function (1-CDF) shown in **Figure 4(b)** provides an integrated view of the void size distribution. This curve represents the probability that a randomly selected void has an effective diameter greater than a given value. The relatively gradual slope of the curve across the range from 0 to 40 μm confirms the multiscale nature of the void architecture, with significant contributions from voids spanning nearly two orders of magnitude in size.

The multimodal void size distribution revealed by this analysis provides quantitative confirmation of the multilevel void structure previously suggested by qualitative observations [8]-[10]. The presence of three distinct void populations with different characteristic sizes and relative abundances reflects the complex interplay between copper electrodeposition and concurrent hydrogen evolution during the synthesis process. Small voids (Peak 1) arise from dendritic branching, intermediate voids (Peak 2) correspond to primary interdendritic spaces, and large voids (Peak 3) result from hydrogen bubble templating effects. This hierarchical porosity is particularly advantageous for electrochemical applications, as it combines high surface area from smaller voids with efficient electrolyte transport pathways provided by the larger interconnected channels.

3.3. Distribution Functions of Fitted Ellipses, Built by Area

The distributions obtained in **Figure 4** effectively describe the void structure from the perspective of quantitative statistics, where each void contributes equally regardless of its size. However, for applications where the volume or area occupied by voids determines functional performance—such as electrolyte access, active material infiltration, or ion transport pathways—it is essential to consider the distri-

bution weighted by the actual space occupied by each void population. Accordingly, the next step was to construct the distribution of interdendritic voids based on their occupied volume (or area, in the case of a two-dimensional image space).

As can be seen from Figure 5(a), the area-weighted data exhibit clear differentiation with several pronounced PDF distribution peaks. Prior to deconvolution, the original probability density function was smoothed to reduce noise arising from the finite number of voids and the discrete nature of the effective diameter binning; this smoothing preserved the overall shape while enabling stable peak fitting. Peak fitting was performed in Origin software using the Gaussian_Loren-Cross peak type, which among the Gaussian-based models, gave the best fit accuracy, reflected in the coefficient of determination ($R^2 = 0.95$). Four peaks were selected based on residual analysis and the requirement to capture all discernible populations without overfitting. The deconvolution parameters are summarized in Table 2.

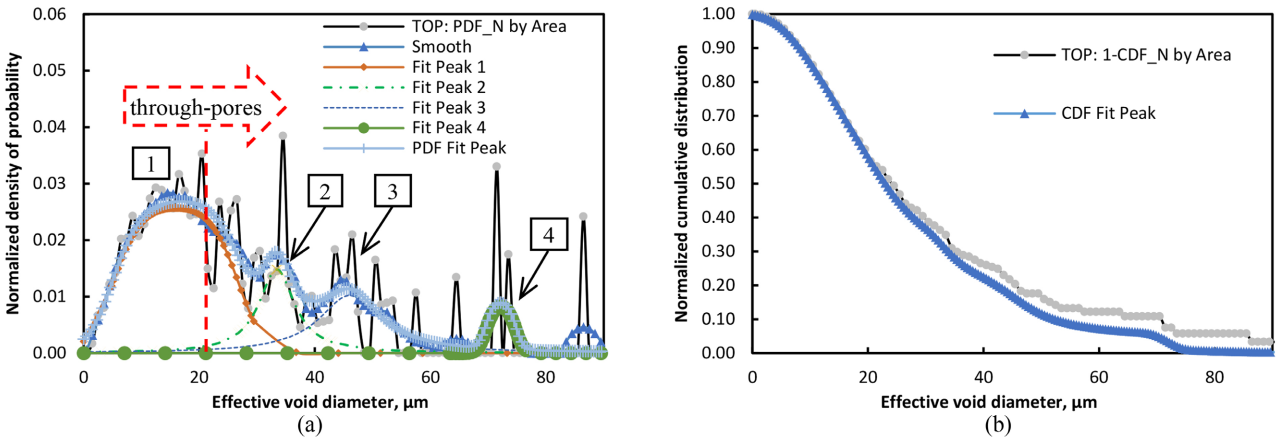

Figure 5. Distribution functions of inscribed ellipses, built by area: (a) Normalized probability density function (PDF) with deconvoluted peaks; (b) Complementary cumulative distribution function (1-CDF).

The deconvolution revealed four distinct populations contributing to the overall void area distribution, with their parameters summarized in Table 2.

Table 2. Deconvolution data summary of area-based PDF.

Peak Number	1	2	3	4
Effective void diameter by peak maximum, μm	15.9	33.4	46.0	72.2
Fraction	0.54	0.16	0.19	0.04
Full width at half maximum (FWHM), μm	21.4	7.5	12.9	5.2
R-sqr (COD)	0.95			

The largest contributions to the total void area come from three primary distribution peaks, though the deconvolution identifies a fourth minor population at larger diameters. The predominant peak (Peak 1), centered at an effective diame-

ter of 15.9 μm, accounts for the majority of the void area with an area fraction of 0.54 (54% of the total void space). This peak exhibits a broad distribution (FWHM = 21.4 μm), indicating that voids in this size class vary considerably in their dimensions while collectively dominating the porous architecture.

The second peak (Peak 2), centered at 33.4 μm with an area fraction of 0.16, represents intermediate-sized voids with a relatively narrow size distribution (FWHM = 7.5 μm). The third peak (Peak 3), centered at 46.0 μm with an area fraction of 0.19, shows a broader distribution (FWHM = 12.9 μm) and contributes nearly as much area as Peak 2 despite being centered at larger diameters. A fourth, minor peak (Peak 4) appears at 72.2 μm with an area fraction of only 0.04 and a narrow distribution (FWHM = 5.2 μm), suggesting the presence of a small population of exceptionally large voids.

A distinct category of through-pores was identified within the dendritic copper layer based on these area-weighted distribution data. Through-pores are defined as voids with an effective diameter equal to or greater than 20 μm, through which the underlying copper substrate surface becomes directly visible in SEM images. This threshold was established empirically, as voids of this size or larger consistently revealed the substrate beneath the dendritic layer during microscopic examination. The formation mechanism of these through-pores is attributed to the coalescence of hydrogen bubbles generated during the hydrogen evolution reaction (HER) at high current densities. As electrolysis proceeds, adjacent hydrogen bubbles merge into larger bubbles that remain attached to the substrate surface for extended periods, effectively blocking copper ion deposition in those regions. This prolonged blocking creates enlarged cavities that penetrate through the entire dendritic layer thickness, establishing direct line-of-sight access to the substrate. The through-pore population is represented by Peaks 2, 3, and 4 in the deconvolution analysis (all peaks with maxima ≥ 20 μm). Collectively, these through-pores occupy approximately 39% of the total void area, calculated by summing their area fractions (0.16 + 0.19 + 0.04 = 0.39). Compared to smaller interdendritic voids, through-pores exhibit significantly enhanced transport characteristics, including improved filtration pathways for electrolyte penetration and substantially reduced diffusion resistance for ion transport throughout the electrode thickness. These larger channels provide low-tortuosity pathways that facilitate rapid electrolyte exchange and promote uniform current distribution during electrochemical cycling.

The cumulative distribution curve (**Figure 5(b)**) demonstrates characteristic volume changes in the regions corresponding to these peak populations. The relatively steep rise in the cumulative curve between approximately 10 μm and 40 μm reflects the dominant contribution of Peaks 1 and 2 to the total void area, while the more gradual increase beyond 40 μm corresponds to the smaller contributions from Peaks 3 and 4.

Comparison between the quantity-based distribution (**Figure 4**) and the area-based distribution (**Figure 5**) reveals important insights into the void architecture.

While the quantity-based analysis identified three populations with peak maxima at 2.41 μm, 5.06 μm, and 10.93 μm, the area-based analysis shifts emphasis toward larger voids. The most numerous voids (Peaks 1 and 2 in Figure 4) are small and contribute minimally to the total void area. Conversely, the voids that dominate by area (Peak 1 in Figure 5, centered at 15.9 μm) are substantially larger, though they represent a smaller fraction of the total void count. This shift reflects the fact that void area scales with the square of diameter, so a small number of large voids can occupy a disproportionately large fraction of the total void space.

The obtained distribution functions effectively describe the void space of a multilevel dendritic structure. The peaks on the curves characterize four key hole sizes, which can be correlated with the three void types conditionally identified in this paper's classification and marked in Figure 3. Peak 1 (15.9 μm) likely corresponds to the primary interdendritic voids formed during the main growth phase. Peaks 2 and 3 (33.4 μm and 46.0 μm) represent larger cavities associated with hydrogen bubble templating effects, where extended periods of bubble blocking created enlarged void regions. Peak 4 (72.2 μm) may correspond to rare, exceptionally large voids formed by coalescence of multiple hydrogen bubbles or extended bubble residence at specific surface sites.

The hierarchical nature of the void architecture is quantitatively confirmed by this analysis. The coexistence of multiple void size classes with different relative contributions to count versus area provides the dendritic copper structure with a combination of high specific surface area (from the numerous small voids) and efficient transport pathways (from the area-dominant larger voids). This multiscale porosity is particularly advantageous for electrochemical applications such as battery current collectors, where both high surface area for reactions and open channels for electrolyte penetration are required.

4. Conclusions

In this work, copper dendritic structures were successfully synthesized by electrocrystallization from a sulfate electrolyte at a high cathode current density of 20 A/dm^2 under conditions of concurrent hydrogen evolution. The obtained deposits are approximately 200 μm in thickness. The multilevel void structure of the synthesized copper dendrites was systematically characterized using scanning electron microscopy combined with advanced image processing and statistical analysis.

The following conclusions can be drawn from this study:

1. The electrodeposition method at high current density with simultaneous hydrogen evolution produces copper dendrites with a highly developed hierarchical pore architecture. The estimated pore density of 2529 pores/mm^2 and the total void area fraction of 0.3054 confirm the formation of an extensive void network within the dendritic structure.
2. Image processing with binary segmentation, watershed separation, and ellipse fitting based on the method of moments provides an effective quantita-

tive approach for characterizing complex dendritic morphologies. This methodology enables objective and reproducible analysis of void structures without the need for specialized and time-consuming characterization equipment.

3. Quantity-based statistical analysis reveals three distinct void populations within the dendritic copper structure. Deconvolution of the probability density function using Gaussian_LorenCross peak fitting identified populations centered at effective diameters of 2.41 μm (23% of voids), 5.06 μm (34% of voids), and 10.93 μm (42% of voids). The excellent fit quality ($R^2 = 0.99$) confirms the validity of the three-population model.
4. Area-weighted analysis provides complementary insight into the distribution of void space, which is critical for understanding transport properties and available surface area. Four void populations were identified, with peak maxima at 15.9 μm, 33.4 μm, 46.0 μm, and 72.2 μm. The predominant contribution comes from voids centered at 15.9 μm, which account for 54% of the total void area despite representing a smaller fraction of the void count.
5. The comparison between quantity-based and area-based distributions reveals the hierarchical nature of the void architecture. Numerous small voids (2 - 11 μm) dominate the pore count and contribute to high specific surface area, while larger voids (15 - 72 μm) dominate the void volume and provide efficient pathways for electrolyte transport. This multiscale porosity is particularly advantageous for battery current collector applications.
6. The average void area of 108.46 μm^2, corresponding to an effective diameter of 11.75 μm, provides a convenient single-parameter representation of the characteristic void size within the dendritic structure. However, this average value alone does not capture the full complexity of the multilevel pore architecture revealed by the deconvolution analysis.
7. The image processing and statistical analysis methodology demonstrated in this work offers a time- and cost-effective alternative to specialized characterization techniques such as physisorption or mercury intrusion porosimetry. This approach can serve as a pre-screening tool to identify promising samples for further detailed electrochemical testing, potentially reducing the resources dedicated to exhaustive characterization of unsuitable specimens.
8. A distinct category of through-pores was identified and characterized within the dendritic copper layer. Through-pores are defined as voids with an effective diameter equal to or greater than 20 μm, through which the underlying copper substrate surface becomes directly visible in SEM images. The formation mechanism of these through-pores is attributed to the coalescence of hydrogen bubbles generated during the hydrogen evolution reaction (HER) at high current densities. As electrolysis proceeds, adjacent hydrogen bubbles merge into larger bubbles that remain attached to the substrate surface for extended periods, effectively blocking copper ion deposition in those regions and creating enlarged cavities that penetrate through the entire dendritic layer

thickness. These through-pores, represented by the deconvoluted peaks centered at 33.4 μm, 46.0 μm, and 72.2 μm in the area-weighted distribution, collectively occupy approximately 39% of the total void area (calculated by summing the area fractions of all void populations with peak maxima ≥ 20 μm: 0.16 + 0.19 + 0.04 = 0.39). Compared to smaller interdendritic voids, through-pores exhibit significantly enhanced transport characteristics, including improved filtration pathways for electrolyte penetration and reduced diffusion resistance for ion transport throughout the electrode thickness. This combination of high surface area from smaller pores and efficient transport through larger through-pores creates an optimized hierarchical architecture for electrochemical applications.

9. While the present study provides a detailed quantitative characterization of the dendritic copper void architecture, several limitations should be acknowledged. The enhanced transport characteristics attributed to through-pores—such as improved filtration pathways and reduced diffusion resistance—are inferred from the 2D morphological analysis rather than confirmed by direct electrochemical testing or three-dimensional structural measurements. Similarly, the operational definition of through-pores ($d_{eff} \geq 20$ μm) is based on visual substrate visibility in SEM images and serves as a practical threshold for classification, but the actual functional relevance of this cutoff in electrochemical applications requires further validation. The porosity metric (total void area fraction = 0.3054) represents a planar projection and may not fully capture the true three-dimensional pore connectivity and tortuosity of the dendritic layer. Complementary techniques such as focused ion beam scanning electron microscopy (FIB-SEM) for 3D reconstruction, X-ray computed tomography, or electrochemical impedance spectroscopy would be valuable to corroborate the transport properties inferred from the present analysis. Notably, the image analysis methodology employed here offers a natural pathway to 3D characterization: by calibrating grayscale intensities in SEM images to actual depth information, the method can be extended to reconstruct the three-dimensional void architecture from a single perspective or stereoscopic pairs. This capability could provide more accurate volumetric parameters without the need for more complex instrumentation. These considerations highlight opportunities for future work to establish direct correlations between the hierarchical void architecture identified here and the electrochemical performance of dendritic copper structures in battery current collector applications.

In summary, the combination of high-current-density electrocrystallization with systematic image-based characterization provides a robust framework for developing and evaluating dendritic copper structures for advanced energy storage applications. The quantitative understanding of void architecture established in this work creates a foundation for correlating synthesis parameters with morphological features and, ultimately, with electrochemical performance in lithium-ion bat-

tery current collectors.

Conflicts of Interest

The authors declare no conflicts of interest regarding the publication of this paper.

References

[1] Younus, H.A., Al Hinai, M., Al Abri, M. and Al Hajri, R. (2024) Copper-Promoted Growth of Hierarchical Cu-Co-Ni Alloys on Copper Nanodendrites for Enhanced Hydrogen Evolution in a Wide pH Range. *International Journal of Hydrogen Energy*, **92**, 247-259. https://doi.org/10.1016/j.ijhydene.2024.10.139

[2] Dixon, E.M., Curtis, N.S., Nagle, L.C. and Rohan, J.F. (2025) Electrochemical Fabrication and Characterisation of Nanoporous Copper from CuZn Alloy Precursors at Macro and Microscale Electrode Arrays. *Electrochimica Acta*, **542**, Article ID: 147487. https://doi.org/10.1016/j.electacta.2025.147487

[3] Guo, F., Yang, B., Lu, W., Peng, X., Zhu, Q., Liu, H., *et al.* (2025) Fabrication of Bilayer High-Strength Nanoporous Copper Current Collector via Electrodeposition-Dealloying. *Journal of Alloys and Compounds*, **1044**, Article ID: 184309. https://doi.org/10.1016/j.jallcom.2025.184309

[4] Liang, Y., Wei, T., Yin, G. and Huang, D. (2025) Design of a Lithiophilic Ag-3D-Cu Electrode and Its Electrochemical Performance. *Energy Storage Science and Technology*, **14**, 515-524. (In Chinese)

[5] Wang, J., Zhou, T., Li, Y., Luo, Z., Liao, X., Wang, X., *et al.* (2025) Growing Mulberry-Like Copper on Copper Current Collector for Stable Lithium Metal Battery Anodes. *Journal of Colloid and Interface Science*, **680**, 129-138. https://doi.org/10.1016/j.jcis.2024.10.200

[6] Colliard-Granero, A., Ranieri, S., Bazylak, A., Morawietz, T., Friedrich, K.A., Jankovic, J., *et al.* (2025) UTILE-Pore: Deep Learning-Enabled 3D Analysis of Porous Materials in Polymer Electrolyte Membrane-Based Energy Devices. *Journal of The Electrochemical Society*, **172**, Article ID: 074515. https://doi.org/10.1149/1945-7111/adf262

[7] Lv, Q., Tian, Z., Li, W., Duan, G., Han, X., Zhang, C., *et al.* (2026) Porous Carbon Derived from Biomass-Based Polymers: Innovative Applications in Supercapacitors. *Chinese Chemical Letters*, **37**, Article ID: 110860. https://doi.org/10.1016/j.cclet.2025.110860

[8] Feng, H., Chen, Y. and Wang, Y. (2017) Multi-Scale Porous Copper Foam Current Collector for High Performance Lithium Ion Battery. *Procedia Engineering*, **215**, 136-144. https://doi.org/10.1016/j.proeng.2017.11.002

[9] Mularczyk, A., Niblett, D., Wijpkema, A., van Maris, M.P.F.H.L. and Forner-Cuenca, A. (2024) Manufacturing Free-Standing, Porous Metallic Layers with Dynamic Hydrogen Bubble Templating. *Advanced Materials Interfaces*, **11**, Article ID: 2400052. https://doi.org/10.1002/admi.202400052

[10] Yang, H., Hao, X., Tang, J., Jin, W., Liu, C., Hou, H., *et al.* (2019) Dual-Functional Porous Copper Films Modulated via Dynamic Hydrogen Bubble Template for *in Situ* SERS Monitoring Electrocatalytic Reaction. *Applied Surface Science*, **494**, 731-739. https://doi.org/10.1016/j.apsusc.2019.07.241

[11] Mulchrone, K.F. and Choudhury, K.R. (2004) Fitting an Ellipse to an Arbitrary Shape: Implications for Strain Analysis. *Journal of Structural Geology*, **26**, 143-153. https://doi.org/10.1016/s0191-8141(03)00093-2

[12] Teague, M.R. (1980) Image Analysis via the General Theory of Moments. *Journal of the Optical Society of America*, **70**, 920-930. https://doi.org/10.1364/josa.70.000920

[13] Severini, T.A. (2005) Elements of Distribution Theory. Cambridge University Press. https://doi.org/10.1017/cbo9780511610547

[14] DasGupta, A. (2010) Fundamentals of Probability: A First Course. Springer.